Journal of Power Sources 344 (2017) 15–24

Contents lists available at ScienceDirect

Journal of Power Sources

journal homepage: www.elsevier.com/locate/jpowsour

Excellent electrochemical performances of nanocast ordered mesoporous carbons based on tannin-related polyphenols as supercapacitor electrodes

A. Sanchez-Sanchez [a, *], Maria Teresa Izquierdo [b], Jaafar Ghanbaja [c], Ghouti Medjahdi [c], Sandrine Mathieu [c], Alain Celzard [a], Vanessa Fierro [a, **]

[a] Institut Jean Lamour, UMR CNRS-Université de Lorraine n°7198, ENSTIB, 27 Rue Philippe Séguin, CS 60036, 88026 Epinal Cedex, France
[b] Instituto de Carboquimica, ICB-CSIC, Miguel Luesma Castan, 4, 50018 Zaragoza, Spain
[c] Institut Jean Lamour, UMR CNRS-Université de Lorraine n°7198, Parc de Saurupt, CS 50840, 54011 Nancy Cedex, France

HIGHLIGHTS

- OMCs successfully synthesised from plant-derived polyphenols through nanocasting.
- Impregnation in one step with no toxic solvents or long polymerisation-stabilisation times.
- Proper replication even for the most bulky precursors (catechin and Mimosa tannin).
- Better electrochemical performances than those for other OMCs or activated carbons.
- OMC from gallic acid showed one of the fastest frequency responses ever reported.

GRAPHICAL ABSTRACT

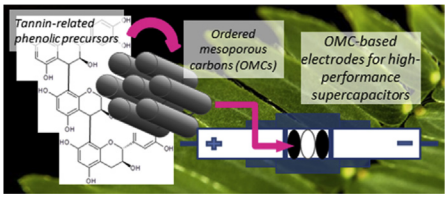

ARTICLE INFO

Article history:
Received 5 October 2016
Received in revised form
1 January 2017
Accepted 22 January 2017

Keywords:
Supercapacitor
Ordered mesoporous carbon
Template method
Phenolic biosourced precursor

ABSTRACT

Hierarchically porous, oxygen-doped ordered mesoporous carbons (OMCs) were synthesised and compared for the first time from different types of plant-derived polyphenols through a nanocasting route: phloroglucinol, gallic acid, catechin and Mimosa tannin. All are secondary metabolites naturally occurring in various plant species and are available at low cost at the industrial scale. The infiltration was carried out in one single step without using toxic solvents or long polymerisation-stabilisation times. When applied as electrode materials for supercapacitors in 1 M H_2SO_4 electrolyte, those OMCs led to specific capacitances up to 277 F g^{-1} at 0.5 mV s^{-1} and high rate capabilities as measured by cyclic voltammetry, good cycling stabilities up to 5000 cycles and maximum energy densities between 15 and 8 W h kg^{-1} under exceptionally high power outputs ranging from 200 W kg^{-1} to 22.1 kW kg^{-1}, respectively, in the range of current density of 0.1–12 A g^{-1}, as determined by galvanostatic charge – discharge. Moreover, electrochemical impedance spectroscopy tests evidenced that the gallic

* Corresponding author.
** Corresponding author.
E-mail addresses: angela.sanchez-sanchez@univ-lorraine.fr (A. Sanchez-Sanchez), vanessa.fierro@univ-lorraine.fr (V. Fierro).

http://dx.doi.org/10.1016/j.jpowsour.2017.01.099

acid-derived electrode exhibited the highest electrical conductivity and the fastest frequency response, making it an excellent candidate for high-power commercial devices.

1. Introduction

Modern society is facing serious environmental problems caused by the use of non-renewable energy sources and, at the same time, needs to meet the growing energy demands to sustain and to boost the technological progress. In this context, it is essential to promote the development of clean energy technologies that can meet the energy and power requirements of portable devices and electric vehicles. Performance and cost of systems for energy storage and conversion limit the effective and widespread use of renewable energy sources. To date, complementary operation of supercapacitors and batteries is the best alternative to supply the required energy in many practical devices [1].

Porous carbon materials have been widely used as supercapacitor electrodes due to their developed porosity, electrical conductivity, availability and moderate cost [2,3]. Among them, ordered mesoporous carbons (OMCs) have attracted increasing attention owing to their regular porous structures, large surface areas and pore volumes, tailored pore size and surface chemistry, mechanical stability and good electrical conductivity [4–6]. Many studies have demonstrated the importance of hierarchical porous structures possessing well-balanced micro- and mesoporosity for enhancing their electrochemical performances. Micropores indeed provide high surface areas for adsorbing electrolyte ions whereas mesopores improve ion transport [4–6]. Moreover, the pore size is a key factor to maximise the electrochemical performance with a given electrolyte [7,8]. Many activated carbons obtained from biomass precursors have been applied as electrodes for supercapacitors but, despite their highly developed porosities and surface areas, electrochemical performances are limited because a large fraction of the porosity is not accessible to the electrolyte [9].

In order to create optimised and tailored porous structures, many synthetic routes and carbon precursors have been investigated [10–13]. Nanocasting, also called nanotemplating or hard-templating method, is a promising route to prepare carbon materials with controlled hierarchical and ordered porous structures by selecting the carbon precursor and the ordered mesoporous silica used as template. Glucose, sucrose, furfuryl alcohol or resorcinol, among others, have been commonly used as carbon precursors for preparing OMCs [14–17]. However, the nanocasting processes using these molecules typically require multiple infiltration steps for completely filling the pores of the template, as well as long polymerisation times and/or the use of toxic reagents.

In the present work, different types of plant-derived polyphenols were used as precursor materials of OMCs. All of them can be potentially extracted from the barks, the fruits, the leaves or the wood of a broad variety of trees [18–21], and are available at low cost at the industrial scale: one monomer of phlorotannins (phloroglucinol), one hydrolysable tannin (gallic acid) and two non-hydrolysable or condensed tannins (monomer: catechin, and oligomer: Mimosa tannin). Out of them, Mimosa tannin is the less expensive precursor, with a cost around 2000 € per metric ton. The OMCs were prepared through a "solid-state thermal polymerisation method" [22], in which the template infiltration was carried out in one single step by simply adding a solution containing the precursor and removing the solvent under vacuum. By simplifying the nanocasting route, the time for obtaining the templated carbon was therefore reduced. To the best of our knowledge, this is the first work using tannin-related polyphenols as precursors for obtaining OMCs through a nanocasting route.

One of the main problems of using bulky molecules in hard-templating is that they can block the entrance of the template pores, thereby preventing the passage of other precursor molecules and giving rise to a final carbon that is a bad replica of the parent silica. In the present work, not only we succeeded in obtaining highly ordered porous OMCs from all the aforementioned tannin-related precursors, but all derived materials also yielded excellent electrochemical performances when applied as electrodes of supercapacitors.

2. Experimental section

2.1. Materials

Pluronic P123 (MW = 5800 Da), tetraethyl orthosilicate (TEOS, 98%), hydrochloric acid (37%), hydrofluoric acid (40%), phloroglucinol, gallic acid, catechin, carbon black powder (<100 nm) and sulphuric acid (1 M) were purchased from Sigma - Aldrich. Mimosa tannin was provided under the name FINTAN OP and was kindly supplied by the company SilvaChimica (St. Michele Mondovi, Italy). Polytetrafluoroethylene (PTFE, 60 wt% in water) and glass fibre mat used as separator were provided by Aldrich and Pall Life Sciences, respectively. All the materials were used as received.

2.2. Preparation of the OMCs

The SBA-15 silica used as template was prepared according to the method of Zhao et al. [23]. In the present work, the molar composition of the starting reaction mixture was 0.017 P123/1 TEOS/145.8H_2O/6.04 HCl. This mixture was stirred at 40 °C for 4 h and subsequently aged at 125 °C for 72 h. The resultant product was filtered and calcined in air at 550 °C for 6 h.

The OMCs were prepared through a hard-templating route based on a method detailed elsewhere [22]. The silica template (1 g) was first degassed under vacuum (150 °C, 2 h). After being cooled down to room temperature, a solution containing the corresponding biosourced precursor (0.01 mol) in ethanol (40 mL) was added to the silica template. Since Mimosa tannin can be composed of oligomers containing typically 2 to 11 monomers, the molecular weight of a single tannin monomer (i.e., prorobinetinidol) was considered to calculate the precursor amount in the solution. The solvent was evaporated under vacuum and the catechin and the Mimosa tannin deposited outside the silica particles were washed off with deionised water. The resultant silica-precursor composites were carbonised in a two-step procedure under nitrogen flow: (i) at low temperature in order to remove the moisture and to polymerise the precursors (100 °C, 2 h dwell time, at 1 °C min^{-1}), then (ii) until the final temperature (900 °C, 1 h dwell time, at 2 °C min^{-1}). The obtained silica-carbon composites were treated with HF for removing the silica, washed several times with deionised water and dried (80 °C, 12 h). The obtained OMCs were labelled PhC, GaC, CatC and TanC, depending on the polyphenol used as precursor in the synthesis: phloroglucinol, gallic acid, catechin and Mimosa tannin, respectively.

2.3. Characterisation techniques

Nitrogen adsorption-desorption isotherms were measured at −196 °C using a Micromeritics ASAP 2020 automatic system, whereas carbon dioxide adsorption isotherms were measured at 0 °C with a Micromeritics ASAP 2420. The surface areas were calculated by applying: i) the BET method to the nitrogen isotherms in the relative pressure interval ranging from 0.05 to 0.35, leading to A_{BET}, and ii) the Non-Local Density Functional Theory (NLDFT) [24] to both nitrogen and carbon dioxide isotherms, leading to S_{DFT}. The Solution of Adsorption Integral Equation Using Splines (SAIEUS®) routine was used to apply NLDFT. The total pore volumes ($V_{0.97}$) were calculated as the amounts of nitrogen adsorbed at a relative pressure of 0.97. The micropore volumes were calculated by applying: i) the Dubinin-Radushkevich (DR) equation to the carbon dioxide isotherms, leading to $V_{\mu\text{-}CO2}$, and ii) the NLDFT model to both the nitrogen and carbon dioxide adsorption isotherms, to determine the pore volume for different pore size ranges, leading to $V_{u\mu\text{-}DFT}$ (<0.7 nm) and $V_{\mu\text{-}DFT}$ (0.7–2 nm). The mesopore volumes, $V_{M\text{-}DFT}$, were calculated by subtracting $V_{\mu\text{-}DFT}$ from $V_{0.97}$.

For each sample, the carbonisation yield was determined as the ratio of the mass of infiltrated silica after pyrolysis to the mass before pyrolysis. Next, the carbon content of the resultant silica-carbon composites was determined with a STA 449F3 Jupiter (NETZSCH) microbalance by heating them under air flow (40 mL min^{-1}) up to the final temperature (900 °C, heating rate 2 °C min^{-1}).

Small-angle X-ray diffraction (XRD) patterns of carbons were recorded with a Panalytical X'Pert Pro diffractometer. The latter was used in a Bragg–Brentano configuration in reflection mode and was equipped with a Cu (Kα radiation) anticathode and a high-speed multichannel X'Celerator detector (scanning range $2\theta = 0.5–3°$; step size = 0.01671°; time per step size = 1.26 s). The unit cell parameter (a, nm) of the carbon mesostructures was calculated by applying Equation (1):

$$a = (2/\sqrt{3}) \times d_{100} \quad (1)$$

where d_{100} (nm) is the interplanar spacing obtained from XRD patterns.

Raman spectra were obtained with a Horiba Scientific XploRa Raman spectrometer. The samples were investigated as received and the spectra were recorded under a microscope using a 100 × objective. The Raman-scattered light was dispersed by a holographic grating with 1200 lines mm^{-1} and detected by a CCD camera. A laser of wavelength 532 nm, filtered at 10% of its nominal power, was used. The incident power (~1.8 mW) was low enough to avoid any heating or damage of the samples. Each spectrum was obtained by accumulation of 2 scans from 800 to 2200 cm^{-1} over 120 s.

Scanning electron microscopy (SEM) and transmission electron microscopy (TEM) images were obtained with FEI XL30 S FEG and Jeol ARM 200F (cold FEG operating at 80 kV) electron microscopes, respectively.

Elemental analysis was performed with an Elementar Vario EL Cube analyser. Carbon, hydrogen, nitrogen and sulphur contents were first determined by combustion of the samples at about 1700 °C (a temperature induced in a furnace, heated at 1150 °C, by a tin foil wrapping the samples and used as catalyst) in a mixed stream of oxygen and helium, the latter being used as carrier gas. Oxygen was quantified with the same equipment in a second step, using a different procedure and another analytic column.

X-ray photoelectron spectroscopy (XPS) results were recorded with an ESCAPlus OMICROM system equipped with a hemispherical electron energy analyser. The spectrometer was operated at 10 kV and 15 mA, using a non-monochromatised MgKα X-Ray source ($h\nu = 1253.6$ eV) and under vacuum (<5×10^{-9} Torr). The hemispherical electron energy analyser operated at the pass energy of 50 eV for survey spectra and at 20 eV for high-resolution spectra. The energy scale was calibrated by referencing the C1s peak to 284.5 eV. The CASA software was used for treating the XPS data.

The electrochemical characterisation was performed with a Biologic VMP3 electrochemical workstation. The carbon electrodes were prepared by mixing the ordered mesoporous carbon material, polytetrafluoroethylene (PTFE, 60 wt% in water) binder and carbon black in the weight percent ratio of 85:10:5 in an agate mortar and drying the resulting paste in an oven (105 °C, 12 h). The dried paste (~3 mg per electrode) was spread onto graphite foils (0.8 cm of diameter) and the resultant supported electrodes were pressed at 5 MPa and impregnated with the electrolyte, 1 M H_2SO_4, at 25 °C and room pressure during 48 h.

Cyclic voltammetry (CV) and galvanostatic charge-discharge (GCD) tests were performed in a three-electrode cell system using the carbon electrode (~3 mg), a platinum gauze as the counter electrode and a saturated calomel electrode (SCE) as reference. Cyclic voltammetry (CV) studies were carried out in the potential window of 0–0.8 V at scan rates ranging from 0.5 to 100 mV s^{-1}. The gravimetric capacitance (C, F g^{-1}) was calculated from the CV curves according to Equation (2):

$$C = (\int I\,\Delta t)/(s\,\Delta V\,m) \quad (2)$$

where I (A) is the current, s (V s^{-1}) is the scan rate, ΔV (V) is the potential window and m (g) is the mass of active material in the electrode.

Galvanostatic charge-discharge experiments (GCD) were carried out in the voltage range 0–0.8 V at charge-discharge current densities ranging from 0.1 to 12 A g^{-1}, based on the total mass of the electrode. From these measurements, the gravimetric capacitance (C, F g^{-1}) was calculated by applying Equation (3):

$$C = (2\,I)/[m\,(dV/dt)] \quad (3)$$

where I (A) represents the discharge current, (dV/dt) (V s^{-1}) the slope of the discharge curve and m (g) the mass of active material in the electrode.

The energy and power densities and the cycling stability were studied in a two-electrode cell in the potential window between 0 and 0.8 V. Symmetrical supercapacitors were assembled by placing two identical electrodes (~3 mg each) separated by a glass fibre separator between two gold current collectors (see Fig. S1 of the Supporting Information section). The energy density (E, Wh kg^{-1}) and the power density (P, W kg^{-1}) were calculated from GCD tests between the current densities of 0.1 and 12 A g^{-1} by applying Equations (4) and (5), respectively. The cycling stability was studied through GCD tests at the current density of 0.5 A g^{-1} up to 5000 cycles; the gravimetric capacitance for a certain GCD cycle and the capacitance retention (%) were determined by using Eq. (3).

$$E = C/8 \times (\Delta V - IR)^2 \quad (4)$$

$$P = E/\Delta t \quad (5)$$

where C (F g^{-1}) represents the gravimetric capacitance calculated from Eq (3) and considering the mass of active material in the two electrodes, ΔV (V) the potential difference within the discharge time Δt (s), and IR (V) the voltage drop due to the inner resistance at the beginning of the discharge process.

Electrochemical impedance spectroscopy (EIS) measurements were performed at open-circuit voltage in a two-electrode system

(mass of each carbon electrode ~ 3 mg) within the frequency range of 100 kHz–1 mHz with a 10 mV alternating current amplitude. The gravimetric capacitance (C, F g^{-1}) was calculated according to Equation (6):

$$C = -2\ \mathrm{Im}(Z)/(\pi f |Z|^2)\ m \quad (6)$$

where $-\mathrm{Im}(Z)$ (Ω) is the imaginary part of the impedance, f (Hz) is the operating frequency, $|Z|$ (Ω) is the impedance modulus and m (g) is the active material mass for the two electrodes.

3. Results and discussion

3.1. Replication of the SBA-15 framework

Fig. 1 illustrates the nanocasting route used for preparing the OMCs presented in this work. Three main steps can be distinguished: i) infiltration, i.e., introduction of the carbon precursors inside the porosity of the silica; ii) carbonisation, i.e., thermal treatment in inert atmosphere after which a silica-carbon composite can be obtained; and iii) leaching, i.e., dissolution of the silica template and recovery of the OMC. As commented above, the templating process is properly accomplished as soon as the pore system of the carbon material is the exact inverse replica of the silica template. Among the precursors used here, phloroglucinol and gallic acid have similar sizes to those of glucose or resorcinol, for example (see Fig. S2 of the Supporting Information section). Using SBA-15 silica with an 8.1 nm mesopore size as template [22], both precursors are expected to be easily introduced inside the pores. The challenge really lies in the introduction of catechin and Mimosa tannin, whose size far exceeds that of one single aromatic ring (see Fig. 1 and Fig. S2). Tannin extracted by infusion of Mimosa bark typically contains from 2 to more than 10 monomers, so that it is difficult to know exactly its molecular weight and size. In fact, silica template may act as a molecular sieve, excluding the penetration within the pores of any molecule possessing a size above a critical value.

The XRD profile of the parent silica presented four well-resolved bands at values of Bragg angle, 2θ, ranging from 0.90 to 2.34° and corresponding to the (100), (110), (200) and (210) reflections (Fig. 2a). The XRD patterns of the derived carbon materials exhibited three peaks assigned to the (100), (110) and (200) reflections in the 2θ interval of 0.94–1.93°. This finding indicates that both the silica template and the carbon replicas possess ordered mesoporous structures belonging to the *P6mm* spatial group [14,23]. The XRD peaks of the carbons displayed in Fig. 2a were shifted to higher angles with respect to those of the SBA-15 silica. The values of interplanar spacing, d_{100}, and of unit cell parameter, a, calculated for the parent silica were 9.80 nm and 11.31 nm, respectively. As shown in Table 1, both values were higher than those obtained for the resultant carbons, suggesting the slight shrinkage of the carbon structure after pyrolysis and removal of the silica template.

The intensity of the XRD bands decreased as the size of precursor molecules increased, which is associated to a gradual decrease of the long-range structural order of the carbons. Large precursor molecules such as catechin and Mimosa tannin can partly block the entry of some silica pores and then prevent the passage of further molecules, or can obstruct the pores so that some gaps can be formed after carbonisation; this explains that the long-range order of the respective carbon materials is partially reduced while keeping a globally ordered arrangement. A previous study on OMCs obtained by chemical vapour deposition of propylene or acetonitrile inside the porosity of SBA-15 silica proved that carbon contents (CC) higher than 24% in the final carbon-silica composite were needed to obtain long-range ordered structures and well-replicated particles after removal of the silica template [25]. Our results agree with this former work, since the tannin-derived OMCs exhibited carbon content values between 24.8 and 40.3% (Table 1).

By considering the product of the carbon content (CC) in the carbon-silica composites and the corresponding carbonisation yield (η_{carb}), CC × η_{carb}, it is possible to obtain information about

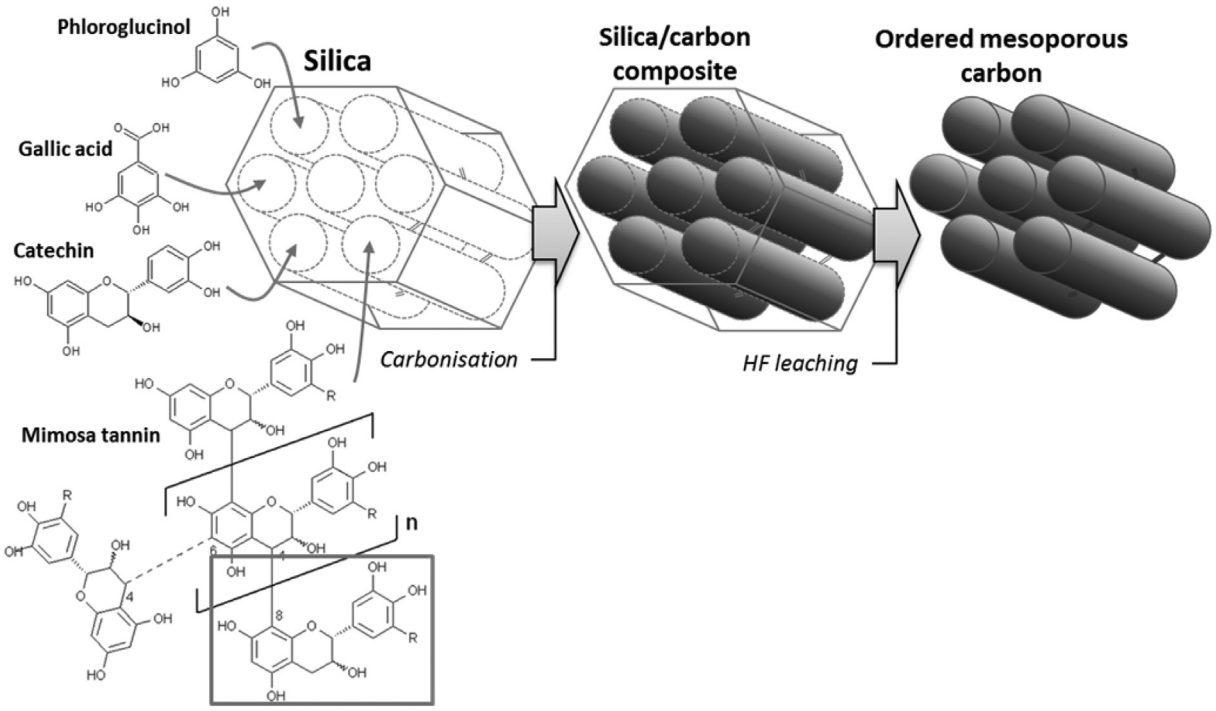

Fig. 1. Schematic procedure for the synthesis of ordered mesoporous carbons (OMCs) through a nanocasting route based on tannin-related carbon sources.

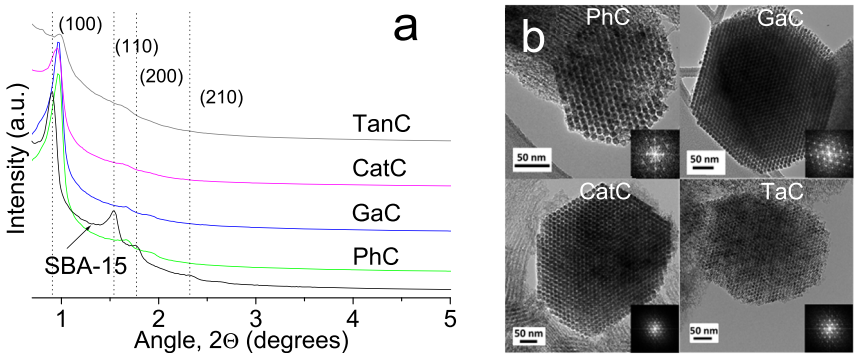

Fig. 2. a) Small-angle X-Ray patterns of parent silica template and derived carbon materials; b) TEM and FFT (inset: Fast Fourier Transform) images of the carbon materials viewed along the cross-sectional direction of the rods.

Table 1
Textural, structural and carbon content data of the studied OMCs.*

Sample	N_2 and CO_2 adsorption isotherms						XRD		TGA	η_{carb} [%][j]	Infiltration degree [%][k]
	A_{BET} [$m^2\ g^{-1}$][a]	S_{DFT} [$m^2\ g^{-1}$][b]	$V_{0.97}$ [$cm^3\ g^{-1}$][c]	$V_{u\mu\text{-}DFT}$ [$cm^3\ g^{-1}$][d]	$V_{\mu\text{-}DFT,0.7\text{-}2}$ [$cm^3\ g^{-1}$][e]	$V_{M\text{-}DFT}$ [$cm^3\ g^{-1}$][f]	d_{100} [nm][g]	a [nm][h]	CC [%][i]		
PhC	1094	1276	1.14	0.17	0.05	0.92	9.17	10.59	36.0	67.6	24.3
GaC	1045	1142	1.03	0.14	0.07	0.82	9.16	10.58	40.3	66.1	26.6
CatC	917	1122	0.87	0.17	0.05	0.65	9.31	10.75	31.6	69.6	22.0
TanC	1006	1196	1.32	0.16	0.01	1.15	9.03	10.43	24.8	80.4	19.9

*Accuracy of the presented data: > 97% for N_2 and CO_2 adsorption data; 99.98% for XRD data; 99.9% for TGA data; 99.9% for carbonisation yields; 99.8% for infiltration degrees.
[a] A_{BET} = BET surface area calculated by applying the BET equation to the N_2 adsorption isotherms.
[b] S_{DFT} = surface area obtained by applying the Density Functional Theory (DFT) to the N_2 and CO_2 adsorption isotherms.
[c] $V_{0.97}$ = total pore volume.
[d] $V_{u\mu\text{-}DFT}$ = ultramicropore volume calculated by applying the DFT model to the N_2 adsorption isotherms.
[e] $V_{\mu\text{-}DFT,0.7\text{-}2}$ = volume of micropores with size between 0.7 and 2 nm, determined by applying the DFT model to the N_2 adsorption isotherms.
[f] $V_{M\text{-}DFT}$ = mesopore volume calculated as $V_{0.97} - (V_{u\mu\text{-}DFT} + V_{\mu\text{-}DFT,0.7\text{-}2})$.
[g] d_{100} = interplanar spacing determined from the (100) peak of the small-angle X-Ray patterns.
[h] a = unit cell parameter calculated from the equation: $a = (2/\sqrt{3}) \times d_{100}$.
[i] CC = carbon content determined by thermogravimetric analysis (TGA) of the silica-carbon composites under air flow.
[j] η_{carb} = carbonisation yield of the silica-carbon composites.
[k] Infiltration degree = CC × η_{carb}.

the infiltration degree of each carbon precursor, expressed in wt.% in Table 1. TanC displayed the lowest infiltration degree, 19.9%, but the highest carbonisation yield, 80%. Taking into account that this carbon exhibited the highest volume of mesopores, 1.15 $cm^3\ g^{-1}$, these data indicate that a heterogeneous infiltration of Mimosa tannin occurred inside the template porosity. This finding is in agreement with the XRD results discussed above.

TEM images of the silica template and of the carbon replicas (Fig. 2b and Fig. S3) show that all these materials possess hexagonal – ordered structures. Keeping in mind the scheme displayed in Fig. 1, it can be asserted that the structure of the resultant carbons is an inverse replica of that of the parent silica: the carbon rods (in black) correspond to the hollow spaces (in white) of the silica structure while the slit-shaped mesopores of the carbon samples (white zones) come from the former silica walls (black zones). TEM images of the OMCs in the longitudinal direction show that mesopores and nano-rods are organised in linear arrays at regular intervals, the latter being the mesopores of size 3–4 nm. Discontinuous carbon rods can sometimes be observed in CatC and TanC (see Fig. S3-f and -g). This indicates that a heterogeneous infiltration took place in the carbons obtained from big-sized precursors, associated to a decrease of the long-range structural order, thus confirming the results obtained from XRD.

The studied carbons exhibited type IV nitrogen adsorption isotherms with sharp capillary condensation steps above the relative pressure of 0.45, characteristic of mesoporous materials, see Fig. 3a and b. H2-type hysteresis loops appeared in the relative pressure range of 0.45–0.60, pointing out the existence of interconnected pores. Those hysteresis loops were associated with narrow pore size distributions (PSDs) centred on ~ 3.4 nm, as shown in Fig. 3c and d. Less-defined hysteresis cycles, similar to H3-type, were also observed above the relative pressure of 0.6, indicating the presence of disordered mesopores larger than 3 nm. This finding was also confirmed by the PSDs collected in Fig. 3c and d, in which mesopores with diameters larger than 4 nm were clearly observed. Thus, the interconnected pores possessing diameters of 3.4 nm correspond to the slit-shaped pores originating from the silica walls that were removed during the leaching step. The disordered, larger mesopores are associated with the porosity generated by a heterogeneous infiltration of the silica template.

A significant fraction of the carbon porosity corresponds to narrow micropores (<0.7 nm), as evidenced by the textural data of Table 1 and the PSDs of Fig. 3c and d: i) $V_{u\mu\text{-}DFT}$ values were much higher than those of $V_{\mu\text{-}DFT,0.7\text{-}2}$; and ii) S_{DFT} values were higher than those of A_{BET} [26]. GaC seemed to exhibit the lowest volume of narrow porosity, since the differences between $V_{u\mu\text{-}DFT}$ and $V_{\mu\text{-}DFT,0.7\text{-}2}$ on the one hand, and between S_{DFT} and A_{BET} on the other hand were slightly lower. The values of surface area decreased when the size of the precursor molecule increased. PhC indeed presented the highest A_{BET} of 1094 $m^2\ g^{-1}$ and one of the highest total pore volume, 1.14 $cm^3\ g^{-1}$. On the contrary, CatC exhibited the lowest A_{BET} values, 917 $m^2\ g^{-1}$, the lowest total pore volume, 0.87 $cm^3\ g^{-1}$, as well as the lowest mesopore volume, 0.65 $cm^3\ g^{-1}$.

SEM images (Fig. 4 and Fig. S3c) of the OMCs and of the silica

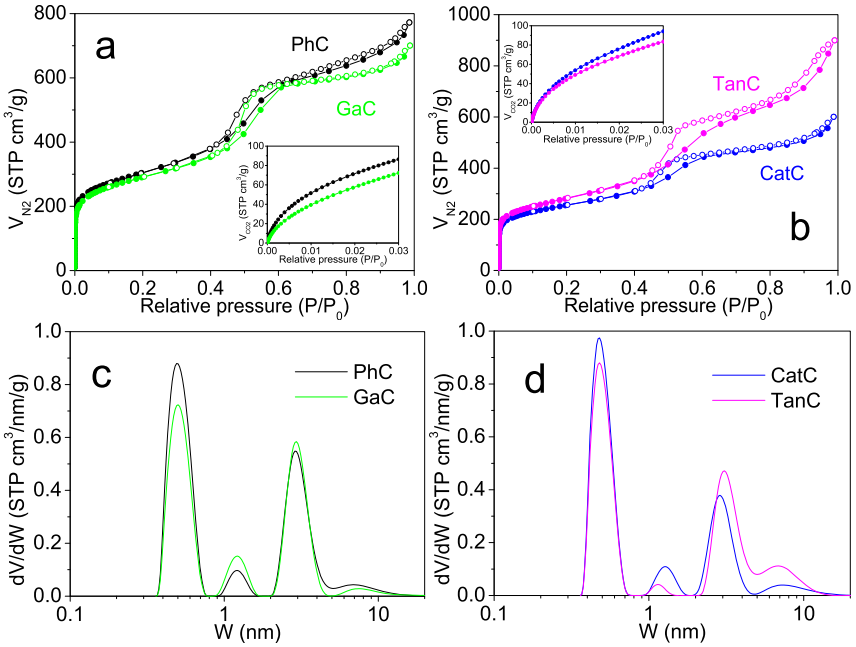

Fig. 3. (a, b) Nitrogen adsorption-desorption isotherms and carbon dioxide adsorption isotherms (insets) of the ordered mesoporous carbons (OMCs); (c, d) corresponding pore size distributions.

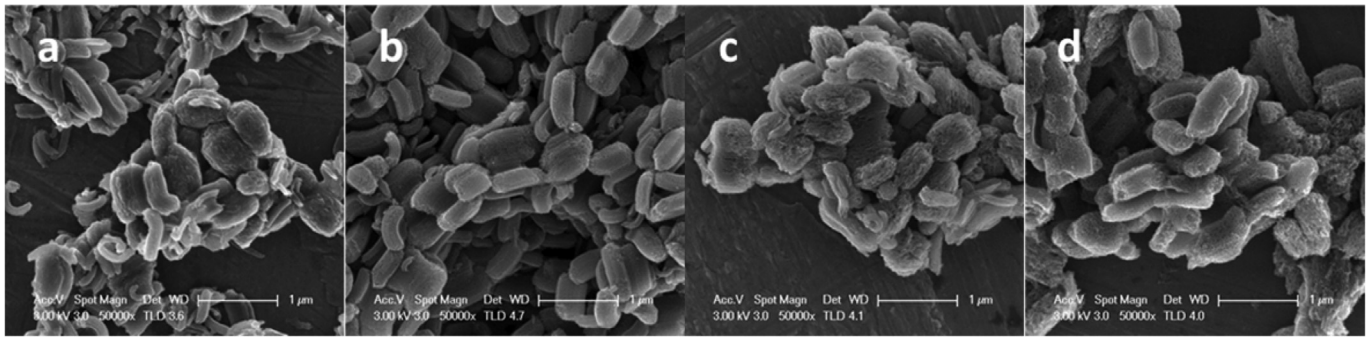

Fig. 4. SEM images of the studied ordered mesoporous carbon materials: a) PhC, b) GaC, c) CatC, and d) TanC.

template evidenced that all these materials were mainly composed of egg-shaped particles with an average size of ~500 nm. Very few incompletely replicated particles were sometimes found in CatC and TanC, as shown in Fig. 4c and d, but these bad replicas were exceptions and are not representative of the whole materials. Thus, it can be considered that, most of the time, the carbon particles were properly replicated from those of the parent silica.

The first-order Raman spectra (from 800 to 2000 cm^{-1}) of the studied OMCs presented D and G bands located at 1334 ± 2 and 1591 ± 6 cm^{-1}, respectively, characteristic of disordered carbon materials (Fig. S4) [27]. The high width and intensity of D bands indicate that the carbons presented a low graphitisation degree and possessed numerous defects and disordered domains [28]. The I(D)/I(G) ratio (I being the intensity of each band) is normally used as an indicator of the density of defects [29]. The calculated I(D)/I(G) values were 0.992, 0.988, 0.976 and 0.955 for PhC, GaC, CatC and TanC, respectively. As these materials are non-graphitisable carbons, the I(D)/I(G) ratio is expected to be proportional to the squared crystallite size, L_a^2 [30]. Therefore, PhC should present the largest crystallites and, hence, it should possess the least disordered nanotexture. Since the order at the atomic level decreased when the molecular size of the precursor increased, it can be assessed that larger precursor molecules are related to a poorer nanotexture order in the studied OMCs.

3.2. Chemical composition

The ultimate composition derived from both elemental analysis

Table 2
Element composition obtained by elemental analysis and XPS.

Sample	Elemental Analysis [wt.%][a]					XPS [wt.%][b]		
	C	N	O	H	S	C	N	O
PhC	87.6	0.2	10.9	1.3	Nd	95.1	Nd	4.9
GaC	90.5	0.3	8.0	1.2	Nd	96.7	Nd	3.3
CatC	87.8	0.2	10.8	1.2	Nd	95.9	Nd	4.1
TanC	89.3	0.5	8.8	1.4	Nd	97.2	Nd	2.8

Nd: Not detectable.

[a] Accuracy for elemental analysis data: 99.5% for C; 64.7% for N; 97.7% for O; 91.9% for H.

[b] Accuracy for XPS data: > 98.0% for C; 90.0% for O. Temperature can change during XPS analysis because of the X-ray source and there is no way to monitor it, but this variation is not a determining factor in the results. Pressure accuracy is deduced from the Bayard-Alpert gauge, being 3% of 5×10^{-9} Torr.

and XPS is reported in Table 2 for each investigated OMC. The results illustrate that oxygen was the main heteroatom both in the bulk and at the surface of the templated carbons. Low nitrogen concentrations, below 0.5 wt%, were also found in the materials bulk, coming from amino acids known to be present as impurities in the precursors and recovered along with polyphenols during their extraction processes. The bulk oxygen concentration was noticeably high, ranging from 8.0 to 10.9 wt%, and decreased to values between 2.8 and 4.9 wt% at the materials surface. It is worth mentioning that oxygen present in the OMCs was unsurprisingly introduced as a natural, abundant element of the precursor molecules, so that no oxidation post-treatment was needed for reaching so high oxygen contents.

The chemical nature of the surface functionalities was investigated by fitting the C1s and O1s high-resolution XPS spectra (Table S1 and Fig. S5). The presence of a broad variety of oxygen functional groups was evidenced: PhC and TanC exhibited the highest relative concentrations of quinone, carbonyl and carboxylic groups, whereas GaC and CatC displayed the highest relative concentrations of phenols, ethers, esters and anhydrides [31–34]. Among the mentioned oxygen functionalities, quinone and carbonyl groups were proved to be electrochemically active in sulphuric acid electrolyte [2,3].

3.3. Electrochemical performances

The CV curves, shown in Fig. 5a, maintained their rectangular shape at sweep rates as high as 100 mV s^{-1}, which indicates an ideal capacitive behaviour allowing fast charge-discharge and ion transport. Slight deviations from the rectangular shape are symptomatic of Faradaic processes of the oxygen functional groups in H_2SO_4 electrolyte. As displayed in Fig. 5b, the highest specific capacitance were obtained for PhC and GaC at 0.5 mV s^{-1} sweep rate, 254 and 277 F g^{-1}, respectively. Such values at low sweep rate exceed those previously reported in the same electrolyte for other OMCs prepared by chemical vapour infiltration of propylene into the porosity of SBA-15 having porosity similar to that of the template used in the present study [35]. In this former work, a symmetric two-electrode cell was used, so the specific capacitances for a single electrode are expected to be lower at the same sweep rate than the values measured here. Oxidised OMCs obtained by soft-templating or resorcinol, phloroglucinol and formaldehyde and subsequent treatment with HNO_3 or ammonium peroxodisulfate (APS) exhibited specific capacitances of 270 and 232 F g^{-1} at 1 mV s^{-1}, respectively, in a three-electrode cell containing 1 M H_2SO_4 [36]. The OMCs studied in the present work therefore led to slightly higher specific capacitances without the need of oxidation post-treatments.

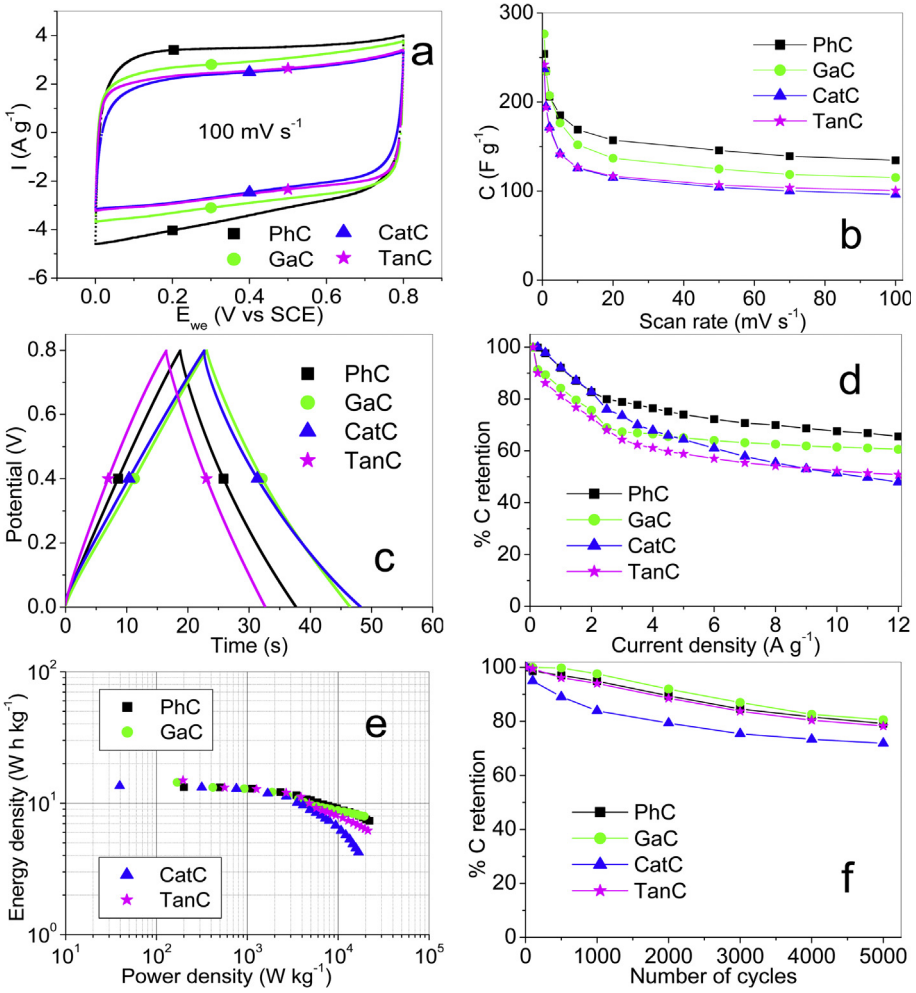

Fig. 5. Results of cyclic voltammetry and galvanostatic charge-discharge tests for OMCs tested in a three-electrode system: a) CV curves at the sweep rate of 100 mV s^{-1} in the potential window of 0–0.8 V; b) Evolution of specific capacitance with scan rate; c) GCD curves at the current density of 1 A g^{-1}; d) Percentage of capacitance retention as a function of current density. Electrochemical performances of the two-electrode system: e) Ragone plot; f) Cycling stability up to 5000 cycles of charge-discharge.

As the scan rate increased from 20 to 100 mV s^{-1}, the capacitance of the OMCs decreased and stabilised to a quasi-plateau, at which the energy storage could mainly occur through a capacitive mechanism. This is explained by the occurrence of incomplete redox reactions taking place at the electroactive functional groups under high-sweep rate regimes [37]. The PhC-based electrode exhibited the highest rate capability since a specific capacitance of 135 F g^{-1} was attained at 100 mV s^{-1}. This value represents 53% of the initial capacitance, higher than the 42% obtained for GaC and TanC, and the 41% of CatC.

The galvanostatic charge-discharge (GCD) curves of PhC, GaC and TanC exhibited quasi-triangular shape with no obvious Ohmic drop at the current density of 1 A g^{-1} (Fig. 5c), pointing out the occurrence of a good electrical conductivity and a preferential electric double-layer storage mechanism [37]. A small Ohmic drop was observed for CatC, suggesting that this material exhibits a higher electrical resistance than the other ones. The slight curvature of the GCD curves evidenced a certain pseudocapacitance contribution originating from redox reactions of the oxygen surface functionalities. At the low current density of 0.1 A g^{-1}, the carbon electrodes yielded similar specific capacitances of ~196 ± 12 F g^{-1}, but those values changed significantly when the current density increased. Thus, capacitance retentions of 65.6, 60.6, 50.8 and 47.9% were obtained at 12 A g^{-1} for PhC, GaC, TanC and CatC, respectively (Fig. 5d).

Energy and power densities are key parameters to evaluate the performance of a certain material when applied as electrodes for supercapacitors. The Ragone plot was drawn from GCD results obtained in a symmetric two-electrode cell within the current density interval between 0.1 and 12 A g^{-1}. The resultant Ragone plot shown in Fig. 5e illustrates that the carbon electrodes yielded similar energy densities of 14.1 ± 0.8 W h kg^{-1} at 0.1 A g^{-1} (the energy density of TanC was almost 15 W h kg^{-1}). At such current density, CatC and PhC exhibited the lowest and the highest power density of 39.4 W kg^{-1} and 200 W kg^{-1}, respectively. The energy densities of the samples remained almost constant up to 1 A g^{-1} and decreased as the current density increased further, being 4.2 and 8.0 W h kg^{-1} at 12 A g^{-1} for CatC and PhC, respectively. The power densities of the materials increased with the current density and reached their highest values at 12 A g^{-1}. At such high current density, PhC had the maximum power density of 22.1 kW kg^{-1}. CatC exhibited lower power density values than the other carbons in the entire investigated current density interval, probably due to a hindered ion transport originating from the presence of many narrow pores.

It is worth noticing that the studied templated carbons exhibited higher energy and power performances than those obtained for a wide variety of materials and electrolytes, such as: OMCs exhibiting BET areas up to 1703 m^2 g^{-1} in 30 wt% KOH (maximum energy density of 4 W h kg^{-1} under the power density of 800 W kg^{-1}) [38]; hierarchical porous carbons with 3000 m^2 g^{-1} surface areas in 1 M Na_2SO_4 electrolyte within the potential range of 0–1.6 V (energy densities of 21.2–10.2 W h kg^{-1} under power outputs of 400 W kg^{-1} – 16 kW kg^{-1}) [39]; activated carbons with 2450 m^2 g^{-1} BET areas in H_2SO_4 electrolyte (maximum energy density values of 7.6 W h kg^{-1} and power density values 4.5 kW kg^{-1}) [40]; activated carbons with BET areas higher than 3800 m^2 g^{-1} in 6 M KOH or 1 M Na_2SO_4 electrolytes (maximum energy densities of 17.4 and 33.6 W h kg^{-1} under the power outputs of 1 and 0.1 W kg^{-1}, respectively) [41]; activated carbons with BET areas up to 2980 m^2 g^{-1} in ionic liquid electrolytes (maximum energy densities of 30 W h kg^{-1} under power densities of 70 W kg^{-1}) [42]. The cycling stability results for the two-electrode systems are shown in Fig. 5f. After 5000 charge-discharge cycles, GaC led to the highest capacitance retention of 80.6%, PhC and TanC presented capacitance retention values of 79.2 and 78.2%, respectively, and CatC exhibited the lowest value of 71.8%.

The high performances of the OMC-based electrodes in regimes of high sweep rates and high current densities confirm that the hierarchical porous structure facilitates the formation of the double-layer thanks to fast ion diffusion within the mesopores and short diffusion distances from mesopores to micropores [43]. The presence of oxygen functionalities has been largely demonstrated to improve the surface hydrophilicity of the carbon electrodes, thereby increasing the interaction with the aqueous electrolyte and enhancing the electrochemical energy storage [36,44]. The higher performances of the PhC-based electrode in terms of specific capacitance, rate capability and higher energy and power densities, compared to the other carbon-based electrodes, can be related to its higher surface area, volume of uniform mesopores and total concentration of surface quinone and carbonyl groups. The higher fading of capacitance observed for the CatC-based electrode might be mainly explained by its porous texture, exhibiting the lowest mesopore volume and the highest volume of narrow micropores, and/or by a low electrical conductivity. The latter was investigated by EIS in a two-electrode cell as follows.

The frequency response of the templated carbons is presented in Fig. 6. The Nyquist plots of Fig. 6a exhibited semicircles at high frequencies (10^5 – 612 Hz) and straight lines at medium - low frequency (26 – 10^{-3} Hz), typical of porous electrodes. 45° Warburg regions were observed in the medium-frequency range (612 – 26 Hz) for the PhC-, CatC- and TanC-based electrodes. The segment length increased in the order PhC < TanC < CatC, indicating increased resistances for ion transport into the electrode bulks.

The absence of Warburg region in GaC suggests an easier diffusion into the pores [45]. This finding agrees with the lower value of electrical distributed resistance (EDR) obtained for GaC

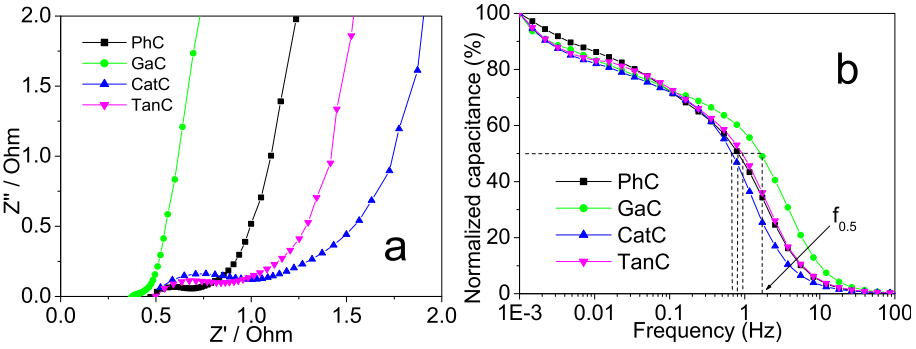

Fig. 6. Results of EIS for all OMCs: a) Nyquist plots; b) frequency responses.

(0.14 Ω), and the higher EDR values obtained for the rest of the materials, between 0.48 and 1.15 Ω for PhC and CatC, respectively. The equivalent series resistance (ESR) of the different cells was calculated from the intercept with the real impedance axis (Z′) of the linear region found at low frequency in the Nyquist plot. ESR includes electrolyte resistance, electrical resistance of the electrodes and contact resistance at the electrode - current collector interface [45]. The GaC-based electrode exhibited the lowest ESR, 0.48 Ω, which means that the corresponding cell presented the highest electrical conductivity. In addition, this ESR value is among the lowest ever reported for OMCs and other carbon materials in aqueous electrolytes, typically higher than 1.0 Ω [39,41,46–49]. The maximal specific capacitances, calculated at 1 mHz, were 215, 199, 183 and 191 F g^{-1} for PhC, GaC, TanC and CatC, respectively. These values follow the same trend already observed for the capacitances calculated by CV and GCD. As expected, the values are not exactly the same because the techniques are different; it is generally known that, for example, CV gives higher values of capacitance than GCD.

The capacitance – frequency dependence of the OMCs (Fig. 6b) suggests that the penetration of electrolyte ions into the pores was hindered in the high-medium frequency regime (10 – 10^5 Hz), since the normalised capacitance decreased when the frequency increased, especially above 1 Hz [45]. If we compare the values of the frequency at which the 50% normalised capacitance is achieved, $f_{0.5}$, it is obvious that GaC exhibited the fastest frequency response with $f_{0.5}$ = 1.1 Hz (only 0.9 s). It is worth noting that most manufacturers do not provide enough information about the parameters needed to determine the frequency-dependent effects. The fastest frequency response of GaC means that lower times are needed to charge or discharge 50% of the full charge of the supercapacitor. To the best of our knowledge, this is one of the fastest frequency responses ever reported, and it can be correlated with the lower volume of narrow porosity, with the high electrical conductivity and with the excellent capacitance retention at both high sweep rates and high current densities. In contrast, CatC displayed the slowest frequency response ($f_{0.5}$ = 0.67 Hz or 1.5 s), i.e., longer times than for the other materials are needed in order to charge or discharge 50% of the full charge of the supercapacitor. This result is in agreement with the correspondingly highest ESR value of the device, the lowest mesopore volume and the presence of a significant fraction of narrow micropores. Anyway, the performances of the polyphenol-derived carbons studied here were clearly higher than those previously reported for a wide variety of OMCs and porous carbon materials [38–42,45].

4. Conclusion

In this work, we have demonstrated that different types of plant-derived polyphenols, and especially tannin-related secondary metabolites (phloroglucinol, gallic acid, catechin and Mimosa tannin), may efficiently be used as biosourced precursors for obtaining OMCs through a nanocasting route. The template structure was properly replicated by means of a single infiltration step, even for the most bulky precursors such as catechin and Mimosa tannin, whose size largely exceeds that of the commonly used molecules. Nevertheless, the smallest molecules, phloroglucinol and gallic acid, allowed obtaining ordered carbons at longer ranges and with slightly higher surface areas. The corresponding OMC-based electrodes exhibited better electrochemical performances in terms of specific capacitances, rate capabilities, and energy and power densities than those of a broad variety of OMCs and commercial or biomass-derived activated carbons previously reported. Moreover, the gallic acid-derived electrode displayed the highest electrical conductivity and one of the fastest frequency responses ever reported so far, making it an excellent candidate for high-power commercial devices.

Acknowledgment

The IJL research team gratefully acknowledges the financial support of the CPER 2007–2013 “Structuration du Pôle de Compétitivité Fibres Grand’Est” (Competitiveness Fibre Cluster), through local (Conseil Général des Vosges), regional (Région Lorraine), national (DRRT and FNADT) and European (FEDER) funds. Part of this work was supported by CHEERS project (FEDER funds). Dr. A. Sanchez-Sanchez acknowledges the University of Lorraine and the Region Lorraine for financing her post-Doctoral contract.

Appendix A. Supplementary data

Supplementary data related to this article can be found at http://dx.doi.org/10.1016/j.jpowsour.2017.01.099.

References

[1] P. Simon, Y. Gogotsi, B. Dunn, Science 343 (2014) 1210–1211.
[2] M. Inagaki, H. Konno, O. Tanaike, J. Power Sources 195 (2010) 7880–7903.
[3] E. Frackowiak, F. Béguin, Carbon 39 (2001) 937–950.
[4] J. Lee, J. Kim, T. Hyeon, Adv. Mater. 18 (2006) 2073–2094.
[5] A. Sanchez-Sanchez, V. Fierro, M.T. Izquierdo, A. Celzard, J. Mater. Chem. A 4 (2016) 6140–6148.
[6] A.S. Arico, P. Bruce, B. Scrosati, J.-M. Tarascon, W. van Schalkwijk, Nat. Mater 4 (2005) 366–377.
[7] J. Chmiola, G. Yushin, Y. Gogotsi, C. Portet, P. Simon, P.L. Taberna, Science 313 (2006) 1760–1763.
[8] E. Raymundo-Piñero, K. Kierzek, J. Machnikowski, F. Béguin, Carbon 44 (2006) 2498–2507.
[9] M. Sevilla, A.B. Fuertes, Carbon 47 (2009) 2281–2289.
[10] A.H. Lu, F. Schüth, Adv. Mater. 18 (2006) 1793–1805.
[11] C. Liang, K. Hong, G.A. Guiochon, J.W. Mays, S. Dai, Angew. Chem. 43 (2004) 5785–5789.
[12] J. Ozaki, N. Endo, W. Ohizumi, K. Igarashi, M. Nakahara, A. Oya, S. Yoshida, T. Iizuka, Carbon 35 (1997) 1031–1033.
[13] T. Kyotani, Carbon 38 (2000) 269–286.
[14] S. Jun, S.H. Joo, R. Ryoo, M. Kruk, M. Jaroniec, Z. Liu, T. Ohsuna, O. Terasaki, J. Am. Chem. Soc. 122 (2000) 10712–10713.
[15] K. Wu, Q. Liu, Appl. Surf. Sci. 379 (2016) 132–139.
[16] M. Kruk, M. Jaroniec, R. Ryoo, S.H. Joo, J. Phys. Chem. B 104 (2000) 7960–7968.
[17] X. Wang, C. Liang, S. Dai, Langmuir 24 (2008) 7500–7505.
[18] S.A. Chowdhury, R. Vijayaraghavan, D.R. MacFarlane, Green Chem. 12 (2010) 1023–1028.
[19] S.J. Cork, A.K. Krockenberger, J. Chem. Ecol. 17 (1991) 123–134.
[20] H.P.S. Makkar, K. Becker, J. Agric. Food Chem. 42 (1994) 731–734.
[21] A. Scalbert, B. Monties, G. Janin, J. Agric. Food Chem. 37 (1989) 1324–1329.
[22] A. Sánchez-Sánchez, F. Suárez-García, A. Martínez-Alonso, J.M.D. Tascón, Carbon 70 (2014) 119–129.
[23] D. Zhao, J. Feng, Q. Huo, N. Melosh, G.H. Fredrickson, B.F. Chmelka, G.D. Stucky, Science 279 (1998) 548–552.
[24] J. Jagiello, J.P. Olivier, Carbon 55 (2013) 70–80.
[25] A. Sanchez-Sanchez, F. Suarez-Garcia, A. Martinez-Alonso, J.M. Tascon, J. colloid interface Sci. 450 (2015) 91–100.
[26] M. Thommes, K.A. Cychosz, A.V. Neimark, Advanced physical adsorption characterization of nanoporous carbons, in: J.M.D. Tascon (Ed.), Novel Carbon Adsorbents, Elsevier Ltd, 2012, pp. 107–145.
[27] V. Barranco, M.A. Lillo-Rodenas, A. Linares-Solano, A. Oya, F. Pico, J. Ibañez, F. Agullo-Rueda, J.M. Amarilla, J.M. Rojo, J. Phys. Chem. C 114 (2010) 10302–10307.
[28] V.N. Tsaneva, W. Kwapinski, X. Teng, B.A. Glowacki, Carbon 80 (2014) 617–628.
[29] D.L. Perry, A. Grint, Fuel 62 (1983) 1024–1033.
[30] A.C. Ferrari, J. Robertson, Phys. Rev. B 61 (2000) 14095–14107.
[31] D. Briggs, in: Surface Analysis of Polymers by XPS and Static SIMS, Cambridge University Press, 1998.
[32] C. Weidenthaler, A.-H. Lu, W. Schmidt, F. Schüth, Microporous Mesoporous Mater. 88 (2006) 238–243.
[33] J.P. Boudou, P. Parent, F. Suárez-García, S. Villar-Rodil, A. Martínez-Alonso, J.M.D. Tascón, Carbon 44 (2006) 2452–2462.
[34] A.B. Dongil, B. Bachiller-Baeza, A. Guerrero-Ruiz, I. Rodríguez-Ramos, A. Martínez-Alonso, J.M.D. Tascón, J. colloid interface Sci. 355 (2011) 179–189.
[35] K. Jurewicz, C. Vix-Guterl, E. Frackowiak, S. Saadallah, M. Reda, J. Parmentier, J. Patarin, F. Béguin, J. Phys. Chem. Solids 65 (2004) 287–293.
[36] S. Tanaka, H. Fujimoto, J.F.M. Denayer, M. Miyamoto, Y. Oumi, Y. Miyake,

Microporous Mesoporous Mater. 217 (2015) 141–149.
[37] D. Wang, Z. Geng, B. Li, C. Zhang, Electrochimica Acta 173 (2015) 377–384.
[38] W. Xing, S.Z. Qiao, R.G. Ding, F. Li, G.Q. Lu, Z.F. Yan, H.M. Cheng, Carbon 44 (2006) 216–224.
[39] H. Zhang, L. Zhang, J. Chen, H. Su, F. Liu, W. Yang, J. Power Sources 315 (2016) 120–126.
[40] A. Jain, C. Xu, S. Jayaraman, R. Balasubramanian, J.Y. Lee, M.P. Srinivasan, Microporous Mesoporous Mater. 218 (2015) 55–61.
[41] C. Long, J. Zhuang, Y. Xiao, M. Zheng, H. Hu, H. Dong, B. Lei, H. Zhang, Y. Liu, J. Power Sources 310 (2016) 145–153.
[42] H. Wang, Z. Li, J.K. Tak, C.M.B. Holt, X. Tan, Z. Xu, B.S. Amirkhiz, D. Harfield, A. Anyia, T. Stephenson, D. Mitlin, Carbon 57 (2013) 317–328.
[43] D.-W. Wang, F. Li, M. Liu, G.Q. Lu, H.-M. Cheng, Angew. Chem. 120 (2008) 379–382.
[44] X. Fan, Y. Lu, H. Xu, X. Kong, J. Wang, J. Mater. Chem. 21 (2011) 18753–18760.
[45] L. Wei, M. Sevilla, A.B. Fuertes, R. Mokaya, G. Yushin, Adv. Energy Mater. 1 (2011) 356–361.
[46] H. Chen, D. Liu, Z. Shen, B. Bao, S. Zhao, L. Wu, Electrochimica Acta 180 (2015) 241–251.
[47] G. Lin, F. Wang, Y. Wang, H. Xuan, R. Yao, Z. Hong, X. Dong, J. Electroanal. Chem. 758 (2015) 39–45.
[48] Y.-Q. Zhao, M. Lu, P.-Y. Tao, Y.-J. Zhang, X.-T. Gong, Z. Yang, G.-Q. Zhang, H.-L. Li, J. Power Sources 307 (2016) 391–400.
[49] J. Zhu, M. Chen, H. Qu, X. Zhang, H. Wei, Z. Luo, H.A. Colorado, S. Wei, Z. Guo, Polymer 53 (2012) 5953–5964.